Contents lists available at Science-Gate

International Journal of Advanced and Applied Sciences

Journal homepage: http://www.science-gate.com/IJAAS.html

An optimal level-set field re-initialization using Chorin's projection method for structured meshes

Umer Siddiqui *, Fahim Raees

Department of Mathematics, NED University of Engineering and Technology, Karachi, Pakistan

ARTICLE INFO

Article history:
Received 26 October 2024
Received in revised form
23 March 2025
Accepted 29 April 2025

Keywords:
Level-set re-initialization
Chorin's projection method
Finite element method
Mass conservation accuracy
Incompressible fluid flow

ABSTRACT

This paper presents a new and effective method for re-initializing the Level-Set (LS) field within the framework of Chorin's projection method. The Navier-Stokes equations (NSE) are solved numerically using the Finite Element Method (FEM) in combination with Chorin's projection method. The proposed approach improves accuracy and efficiency, ensuring precise mass conservation of the LS field. The effectiveness and efficiency of the re-initialization method are validated through benchmark test cases. This study provides an efficient approach for solving time-dependent incompressible fluid flow problems by using Chorin's projection method to separate pressure and velocity fields. Additionally, it introduces an efficient technique for re-initializing the LS field. The findings demonstrate the accuracy, efficiency, and mass conservation capabilities of the method, making a valuable contribution to numerical analysis and computational fluid dynamics.

1. Introduction

The flow in which multiple phases coexist simultaneously, such as solid, liquid, or gas, is described as multiphase flow. Multiphase flow is crucial in several industrial processes and numerous fields, including environmental engineering, petroleum engineering, and chemical engineering. Two prominent methods study the multiphase flow: (i) the Eulerian-Eulerian method and (ii) the Eulerian-Lagrangian method. Both methods facilitate the exchange of phenomena associated with turbulence, momentum, mass, and heat transfer.

The multiphase flow comprises four main types: (i) solid-liquid flow, (ii) solid-gas flow, (iii) liquid-gas flow, and (iv) liquid-liquid flow. In a multiphase flow, material characteristics and the two-phase effects, e.g. density and viscosity, significantly influence the interface's movement. Multiphase flow has numerous applications, including nuclear engineering, environmental engineering, oil and gas industries, biomedical treatment, chemical processes, medical sciences, mining and mineral processing, food and beverage industries, and infrastructure and transportation.

Multiphase flow presents several prominent challenges; these include the scalability of phase distribution, mass and heat transfer computational complexity, flow regime transitions, and system design. Recently, various models have emerged for multiphase flow simulation, including computational fluid dynamics (CFD), separated flow, multi-fluid, homogeneous, and drift-flux models. Researchers have introduced several creative methods for multiphase flow simulation: Level-Set (LS) method (Osher and Sethian, 1988), the Volume of Fluid (VoF) method (Hirt and Nichols, 1981), the Marker Particle (MP) method (Rider and Kothe, 1995), and the Modified Level-Set (MLS) method (Owkes and Desjardins, 2013).

The projection method was introduced by Chorin (1967). He has made significant contributions to computational fluid mechanics (CFM), turbulence modeling, and computational statistical mechanics (CSM). The framework of the projection method relies on the Helmholtz decomposition, which separates the velocity field into two components: (i) a solenoidal (divergence-free) part and (ii) an irrotational (curl-free) part, as discussed in Chorin and Marsden (1990).

The numerical approaches, devised for the Navier-Stokes equations (NSE) experience difficulty with the incompressibility limitation (Yang et al., 2024). Akbar et al. (2022) introduced the first

* Corresponding Author.
Email Address: siddiquiumer@ymail.com (U. Siddiqui)
https://doi.org/10.21833/ijaas.2025.05.007
Corresponding author's ORCID profile:
https://orcid.org/0009-0000-2269-0450

primitive-variable numerical approach, applying the incompressibility limitation through pressure obtained with the derivation of the Poisson equation by getting the divergence of the equation of motion for the incompressible viscous fluids shown in (Chorin, 1997). Nevertheless, the pressure does not specify the physical conditions, necessitating unnatural boundary conditions, which add complexity to the problem. Gresho and Sani (1987) examined the relation between the dissimilar pressure boundary conditions and the actual equations.

The combined set of equations is non-trivial for solving pressure and displacement in a linear system. The fixed-stress splitting method discussed in Dana et al. (2021) is extensively used to solve these equations. It solves the mechanical difficulties in the order. One can create the equations of motion in two views: (i) the Lagrangian approach and (ii) the Eulerian approach given in Derr and Rycroft (2022). The Lagrangian approach traces variables at a specified material point, whereas the Eulerian approach traces variables within the selected point of space. The Lagrangian composition traces displacement and fluid flux at all material points, whereas the Eulerian approach traces the density and momentum at time steps within a specified point of space. Investigators have also examined these approaches for porous media flow, which relies on uncomplicated geometry and actual solutions.

MAC grids are very advantageous to discretize the grad/div as stop pressure discussed in Gagniere et al. (2020). Several coupled finite element methods (FEM) collect velocities lacking the uncertainty of pressure. For instance, the Taylor-Hood elements method (Gharibi and Dehghan, 2024) interpolates multi-quadratic velocity and multi-linear pressure with incompressibility. The Taylor-Hood method (Bressan, 2011) interpolates the B-spline approach (de Boor, 1978). The collected velocities are employed using the pressure at the cell centers. The certainty of the collected grids is encouraged. However, the B-Spline approach achieves continuous derivatives quickly.

An American scientist invented the initial variant of the projected method as in Long and Ding (2023) and is employed extensively due to its efficacy and clarity. The projection method solves the separated equations for pressure and velocity at each time interval. It is an impressive characteristic of the projection method, and this method is successful for considerable numerical imitations. The projection method depends upon the time-discretization scheme, which is effective in iteratively estimating the pressure and velocity field intellectually at every time interval. Researchers have studied several projection methods in temporal discretization related to error analysis in recent decades. Rannacher (1992), as discussed in Karam and Saad (2023), improved the computation of first-order optimal error estimates through derivations related to the original projection method (Guermond and Shen, 2004; Bir et al., 2024).

The Chorin–Temam projection approach, a widely recognized method, has been extensively studied. The constancy of this approach, as discussed in Guermond and Quartapelle (1998) and Guermond and Shen (2004), is further elaborated in Codina (2001). The non-inf-sup finite elements approximate the pressure and velocity and achieve several deducible bounds. However, the researchers did not test the bounds of errors for this approach. The Chorin–Teman approach is examined in Badia and Codina (2007) using the inf-sup and non-inf-sup combined finite elements. The local kind of projection stability is requisite with the non-inf-sup firm combined finite element to achieve the bounds of error of the approach. The researchers attain optimum error bounds (de Frutos et al., 2018) with no other stability used in non-inf-sup firm combined finite elements.

The Navier-Stokes equations are solved numerically using the projection methods formulated by Han et al. (2023). The first level of the projection schemes estimates the intermediate velocity by solving the momentum equation without the divergence-free incompressibility constraints. In the second level of the projection scheme, the intermediate velocity assists to obtain the final velocity upon divergence-free space. Unfortunately, that velocity field fails to meet the boundary conditions. This method is supposed to be 'The error of the splitting approach" (Jobelin et al., 2006). Compared to other approaches, the outcomes are less accurate. A splitting dimension error can determine the magnitude of the intermediate velocity. In this paper, a new effective re-initialization for the LS) field within the framework of Chorin's projection method. The Finite Element Method (FEM) is used to numerically solve the NSE using Chorin's projection method. The proposed scheme demonstrates enhanced proficiency and effectiveness, ensuring accurate mass conservation of the Level-Set (LS) field. Benchmark test cases will validate the proposed scheme's significance, efficiency, and effectiveness of the presented re-initialization scheme.

This connection presents a new method to solve the incompressible fluid flow time-dependent issues. Using Chorin's projection method, we separated the fluid's pressure and velocity field and added the re-initialization scheme for the LS re-initialization. In this research, we provide an accurate and efficient solution to the NSE.

The main goal of the presented method is to enhance the competence, efficiency, and mass conservation capability in an NSE solution, which is solved numerically. The FEM is employed to increase the sturdiness of the numerical technique. Adding the re-initialization method using Chorin's projection method constitutes a new development in the field, which provides better accuracy and competence to solve incompressible fluid flow time-dependent issues.

The re-initialization method based on Chorin's projection is preliminarily devised for structured meshes. Regardless, we can also adjust LS re-initialization for unstructured meshes, but it uses more intricate data structures and numerical procedures to regulate the inconsistent connectivity of the complex geometries. A specific error analysis of the LS re-initialization method with Chorin's projection method demonstrates its convergence rate associated with mesh enhancement. The scheme naturally reveals second-order precision for smooth solutions. Numerical errors may influence this exactness, particularly close sharp interfaces or areas with abrupt gradients.

We organize the paper's outline as follows: section 2 illustrates the Level-Set method, Section 3 explains the re-initialization method, and Section 4 discusses the test results. The last section (section 5) presents the conclusion of this research.

2. The level-set method

The two American scientists Osher and Sethian (1988) introduced an interface-catching technique named The Level-Set method. The interface finding in the LS method is highly straightforward; however, this technique faces the difficulty of mass conservation. Hence, the LS method is much superior to the other interface-catching methods. Naturally, using the partial differential result depicts an interface. The least insignificant idea is to demonstrate the interface entirely using zero-LS, revealed within the two and three dimensions.

In a two-dimensional instance, we suppose that the function $\Gamma(t)$ represents the interface (or in a three-dimensional surface) bounded across the region $\Omega \in \Re^2$ (It is not necessary to open the bounded area.). The motivated interface vector field $\mathbf{V} = (v_1, v_2)$ uses the interface motion that depends upon the place of an interface, time, and the shape of the interface.

The main framework of the LS method is illustrated in the above section using the function of LS $\phi = (x, y, t)$ within the one and higher-dimensional test instances. The LS method's paramount attitude is that the LS value is negative on the interface bottom and positive on the interface top, and the sign will remain stationary over the interface, showing the contour at zero as $\phi = (x, y, t)$. The present position of the interface $\Gamma(t) = \{(x, y) \mid \phi(x, y, t)\}$ is always at zero using their contours. In a conservative form, we can write the equation of the LS in the mathematical form as follows over the divergence-free velocity field given in Ausas et al. (2008), delving into the intricate mathematical representation of the LS method.

$$\frac{\partial \phi}{\partial t} + \mathbf{V} \cdot \nabla \phi = 0 \tag{1}$$

where, $\frac{\partial \phi}{\partial t}$ indicates the variation in the interface with time t. $\mathbf{V}$ constitutes the velocity field whose divergence is equal to zero i.e. $\nabla \cdot \mathbf{V} = 0$ and $\nabla \phi$ represents the LS function's gradients from an interface.

Naturally, the function of the LS upholds the property of the signed distance mathematically expressed as $|\nabla \phi| = 1$, and ϕ demonstrates the function of the interface's sign distance. In the two and three-dimensional scenario of the LS method, the size of the function of sign distance is as:

$$\sqrt{\phi_x^2 + \phi_y^2} \tag{2}$$

$$\sqrt{\phi_x^2 + \phi_y^2 + +\phi_z^2} \tag{3}$$

where, in Eqs. 2 and 3, x and y indicate the course of the LS function. Fig. 1 depicts an instance of the LS method and its contour.

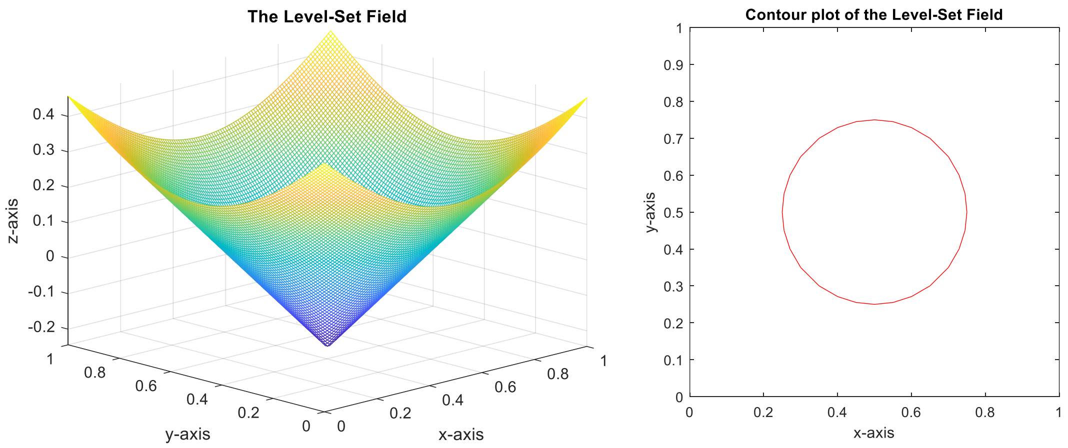

Fig. 1: The instance of the LS method and its contour

In the image processing area, the Chan-Vese segmentation (Chan and Vese, 2001) discussed by Khan et al. (2020) has vigorous contours devoid of edges. The LS method solves the Chan-Vese segmentation efficiently. This segmentation can be switched into an easier form using the LS method. In three components, segmentation divides the area into (i) the starting boundary, (ii) the exterior border, and (iii) the interior border. Researchers found that above the border, the LS value is zero, positive inside an interior border and negative inside an exterior border. Researchers have used various methods, including the checkerboard method

(Zhang, 2014). This method ascertains the LS function and relies on thresholding.

The LS approach enhances Hamilton-Jacobi equations for enhancing the LS function, creating substantial slopes near the boundaries. The poor accuracies of the LS functions generate an infirm approximation of the usual boundary values. In the re-initialization process, the gradient accuracy of the LS function retains the signed distance function. The FEM shape functions perform small iterations approximating the zero LS (iso-contour). Later, the discredited iso-contour distances are computed. The LS approach manages complex changes in topology during re-initialization; however, the complete solution of the conventional LS approach relies on initial shapes during the advancement of the structural optimization issues in two dimensions.

The advancement of the LS method is exploited by Lyras et al. (2020) for the continuous function to understand the Volume of Fluid (VoF) method. In particular, the LS method accurately depicts an interface's curvature. Both the LS and VoF methods experience complexities in geometry. The main dissimilarity between the two methods is that the LS method's fluid passage is slower than the VoF method; the LS method catches the interface effortlessly; however, it needs mass conservation. The LS method must be combined with the VoF method to resolve the mass conservation issue.

3. Re-initialization method

In this portion, we discuss the LS method re-initialization, which is studied in this paper to re-initialize the LS function. Normally, the LS method's issue of re-initialization emerges because it does not properly conserve the mass. Several methods have been provided in the last decades to overcome this complexity, namely the re-initialization scheme based on partial differential equation (PDE) (Hartmann et al., 2008), the mass-conserving re-initialization method based on geometry (Ausas et al., 2008), and etc.

The geometric-based re-initialization method is illustrated here and employs the conception of the finite element method (FEM) for the re-initialization. The idea for the re-initialization for the LS method is that a second-degree polynomial has fitted over the rectangular shape element of a domain and determined the minimal distance from the interface to each node of all rectangular shape elements over the domain. We observe that the LS cost will not change its signs over the interface; the LS costs will vary at the bottom and top of the interface, i.e. $sign\ (\phi)$, in this expression, ϕ denotes the LS costs and the sign indicates the signs (negative or positive) of the LS costs from the interface. Later, we estimate the minimal distances from the interface to the nodes of all elements; after that, the new updated LS costs are,

$$\phi' = sign(\phi) \cdot d \tag{4}$$

where, in Eq. 4 the new updated LS value is represented by ϕ', d represents the minimal distance from the interface to the nodes of all elements in a domain, and ϕ are the costs of actual LS. In the study of the FEM, the polynomial equation for the quadrilateral element expresses as:

$$\phi\ (x, y) = \sum_{i=1}^{4} N_i\, \phi_i \tag{5}$$

where, $N_i = 1 \leq i \leq 4$ are the shape functions of the quadrilateral element and $\phi_i = 1 \leq i \leq 4$ are the actual LS costs over that element. The costs of the shape functions are,

$$N_i = \frac{(x-x_j)\,(y-y_k)}{(x_i-x_j)\,(y_i-y_k)} \quad i \neq j \neq k$$
$$1 \leq i \leq 4, 1 \leq j \leq 4, 1 \leq k \leq 4 \tag{6}$$

where, $(x,\ y)$ are the point coordinates inside the element and i, j, k are its indices in Eq. 6, and they are different from each other and will cover four different element nodes.

The solution of the Eq. 5 is written as:

$$\phi\ (x, y) = \beta_0 x + \beta_1 xy + \beta_2 y + \beta_3 + \beta_4 x^2 + \beta_5 y^2 \tag{7}$$

where, $\beta_0, \beta_1, \beta_2, \beta_3$ are the constant values per element in Eq. 7 and $\beta_4 = \beta_5 = 0$ because of the element's Orthogonality.

For the re-initialization procedure, consider the NSE and employ Chorin's projection method to solve NSE with boundary conditions $\mathbf{u} = 0$ over the boundary with computational domain $\Omega = [0\,, 1] \times [0\,, 1]$ to get the fluid's pressure. We utilize the estimated pressure to acquire the final velocity at n + 1-time intervals

3.1. Process of re-initialization

In the re-initialization process, we use the FEM together with the Lagrange multiplier method. Employ the FEM for solving Eq. 5. Later, the distance formula determines the minimal distances from the interface to every node of the quadrilateral element by the Lagrange multiplier method. Mathematically, the distance formula is as follows:

$$|\ d\ | = \sqrt{(x_l - x_L)^2 + (y_l - y_L)^2}\ ,\ 1 \leq L \leq 4 \tag{8}$$

where, d is the shortest distance from the interface, x_l and y_l are the node's coordinates, and x_L and y_L are the points on the interface represented as $\phi\ (x, y) = 0$.

3.2. Working of the re-initialization method

In the working of the re-initialization scheme, we examine the quadrilateral element with coordinates $\underline{\mathbf{X}}_i = 1 \leq i \leq 4$, with corresponding shape functions $N_i = 1 \leq i \leq 4$ along with LS costs $\phi_i = 1 \leq i \leq 4$ shown in Fig. 2.

We presume that the LS cost ϕ_1 is for the first node $\underline{\mathbf{X}}_1$, ϕ_2 is for the second node $\underline{\mathbf{X}}_2$, ϕ_3 is for the third node $\underline{\mathbf{X}}_3$ and ϕ_4 is for the fourth node $\underline{\mathbf{X}}_4$, respectively. We fitted the second-degree polynomial over the quadrilateral element and determined the minimal distance from the interface where the polynomial cost equals zero represented as $\phi\,(x, y) = 0$ Using the Lagrange method of the multiplier approach, we determined the minimal distances from the interface since the function needs to be minimized so that $\phi\,(x_m, y_m) = 0$.

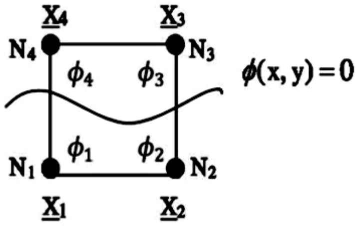

Fig. 2: Schematic plot of all nodes of the quadrilateral element

3.3. Derivation of the Lagrange method of multiplier approach

For the illustration of the Lagrange multiplier method, we examine the optimization Scenario.

Minimize $d(x, y)$
Subject to $\phi\,(x, y) = 0$

where, $d(x, y)$ represents the distance function and $\phi\,(x, y)$ is denoted as the LS function. We presume that the partial derivatives are continuous of both $d(x, y)$ and $\phi\,(x, y)$. Now, introduce a new variable λ called the Lagrange multiplier, exemplified as:

$$\mathcal{L}(x, y, \lambda) = d(x, y) + \lambda \cdot \phi\,(x, y) \tag{9}$$

In Eq. 9, we can add or subtract the expression λ.

$$M(x_m, y_m) = d(x_m, y_m) + \lambda \cdot \phi\,(x_m, y_m) \tag{10}$$

where, $N = d^2 = (x_m - x_l)^2 + (y_m - y_l)^2$, $1 \leq l \leq 4$ and $\phi\,(x_m, y_m) = \beta_0 x_m + \beta_1 x_m y_m + \beta_2 y_m + \beta_3 = 0$, x_m *and* y_m.

In the above relation, x_m and y_m are the familiar points, x_l and y_l unfamiliar points respectively,

$$(x_m, y_m) = \beta_0 x_m + \beta_1 x_m y_m + \beta_2 y_m + \beta_3 = 0 \tag{11}$$

In Eq. 11, $\beta_0, \beta_1, \beta_2, \beta_3$ are the equation's coefficients and they have constant values, which can be positive or negative on each quadrilateral element.

$$\frac{\partial M}{\partial x_m} = \frac{\partial N}{\partial x_m} + \lambda \frac{\partial \phi}{\partial x_m}$$

$$\frac{\partial M}{\partial x_m} = 2(x_m - x_l) + \lambda(\beta_0 + \beta_1 y_m) = 0 \tag{12}$$

After simplification, Eq. 12 can be rearranged as:

$$2x_m + \lambda\beta_1 y_m = 2x_l - \lambda\beta_0 \tag{13}$$

$$\frac{\partial M}{\partial y_m} = \frac{\partial N}{\partial y_m} + \lambda \frac{\partial \phi}{\partial y_m}$$

$$\frac{\partial M}{\partial y_m} = 2(x_m - x_l) + \lambda(\beta_2 + \beta_1 x_m) = 0 \tag{14}$$

After simplification, Eq. 14 can be rearranged as:

$$\lambda\beta_1 x_m + 2y_m = 2y_l - \lambda\beta_3 \tag{15}$$

$$\frac{\partial M}{\partial \lambda} = \frac{\partial N}{\partial \lambda} + \lambda \frac{\partial \phi}{\partial \lambda}$$

$$\frac{\partial M}{\partial \lambda} = \phi\,(x_m, y_m) = \beta_0 x_m + \beta_1 x_m y_m + \beta_2 y_m + \beta_3 = 0 \tag{16}$$

$$\beta_0 x_m + \beta_1 x_m y_m + \beta_2 y_m + \beta_3 = 0 \tag{17}$$

We obtain point $\underline{\mathbf{I}}$ on the interface after solving Eq. 13 and Eq. 15, we have:

$$\underline{\mathbf{I}}\,(x_m, y_m) = \left(\frac{4x_l - 2\lambda\beta_1 y_l - 2\lambda\beta_0 + \lambda^2\beta_1\beta_2}{(4 - \lambda^2\beta_1^2)}, \frac{2x_1\lambda\beta_1 - \lambda^2\beta_0\beta_1 - 4y_l + 2\lambda\beta_3}{-\,(4 - \lambda^2\beta_1^2)}\right) \tag{18}$$

where, x_m and y_m are the coordinates of point $\underline{\mathbf{I}}$ lying on the interface. Substituting the coordinate's costs of $\underline{\mathbf{I}}$ in Eq. 17 we have:

$$\beta_0 x_m + \beta_1 x_m y_m + \beta_2 y_m + \beta_3 = 0$$

After substituting the costs of x_m and y_m in Eq. 17, the Eq. 17 is simplified as:

$$(\beta_3\beta_1^4 - \beta_0\beta_1^3\beta_2)\,\lambda^4 + 0\,\lambda^3 + (4\beta_1^2\beta_2 y_l + 12\beta_0\beta_1\beta_2 + 4\beta_1^3 x_l y_l + 4\beta_1^2\beta_0 x_l - 8\beta_3\beta_1^2)\,\lambda^2 + \left(-8\beta_1^2 x_l^2 - 8\beta_0^2 - 16x_l\beta_1\beta_2 - 8\beta_2^2 - 16\beta_0\beta_1 y_l - 8\beta_1^2 y_l^2\right)\lambda + 16\beta_0 x_l + 16\beta_1 x_l y_l + 16\beta_3 + 16\beta_2 y_l = 0 \tag{19}$$

Therefore, the final structure of Eq. 18 is:

$$\Psi_0\,\lambda^4 + \Psi_1\,\lambda^3 + \Psi_2\,\lambda^2 + \Psi_3\,\lambda + \Psi_4 = 0 \tag{20}$$

where,

$$\Psi_0 = \beta_3\beta_1^4 - \beta_0\beta_1^3\beta_2$$
$$\Psi_1 = 0$$
$$\Psi_2 = 4\beta_1^2\beta_2 y_l + 12\beta_0\beta_1\beta_2 + 4\beta_1^3 x_l y_l + 4\beta_1^2\beta_0 x_l - 8\beta_3\beta_1^2$$
$$\Psi_3 = -8\beta_1^2 x_l^2 - 8\beta_0^2 - 16x_l\beta_1\beta_2 - 8\beta_2^2 - 16\beta_0\beta_1 y_l - 8\beta_1^2 y_l^2$$
$$\Psi_4 = 16\beta_0 x_l + 16\beta_1 x_l y_l + 16\beta_3 + 16\beta_2 y_l$$

Eq. 20 represents the Quartic equation in the form of λ, we employ the costs of λ to compute the minimal distance from the interface to each node of the quadrilateral element. If all the roots of the equation are complex in this situation, substitute the shortest or minimum distances with the actual LS costs (ϕ).

3.4. Projected velocity field using Chorin's projection method

Generally, the projection method framework relies on the Helmholtz decomposition principle, which divides the velocity field u into two portions: (i) the irrotational portion $\mathbf{u}_{irrot}$, and (ii) the solenoidal portion $\mathbf{u}_{sol}$. Mathematically we have:

$$\mathbf{u} = \mathbf{u}_{sol} + \mathbf{u}_{irrot} \tag{21-a}$$
$$\mathbf{u} = \mathbf{u}_{sol} + \nabla\phi \tag{21-b}$$

We know that from the Vector Calculus $\mathbf{u}_{irrot} = \nabla\phi$. Taking divergence on both sides of Eq. 21-b we have:

$$\nabla \cdot \mathbf{u} = \mathbf{u}_{sol} + \nabla \cdot \nabla\phi \quad \therefore \{\mathbf{u}_{sol} = \nabla \cdot \mathbf{u} = 0 \Rightarrow \nabla \cdot \mathbf{u}_{sol} = 0 \tag{22-a}$$
$$\nabla \cdot \mathbf{u} = 0 + \nabla^2\phi$$
$$\nabla \cdot \mathbf{u} = \nabla^2\phi \tag{22-b}$$

The Eq. 22-b represents the Poisson equation for the scalar function and the solution of Eq. 22-b was easily obtained, leveraging the known velocity field $\mathbf{u}$ for ϕ.

The divergence-free potion was removed for the velocity field $\mathbf{u}$ by employing the relation defined in Eq. 23 using Eq. 21-b as:

$$\mathbf{u}_{sol} = \mathbf{u} - \nabla\phi \tag{23}$$

This paper applies Chorin's projection method to re-initialization process, as discussed in Section 3. Chorin's method disassociates pressure and velocity and describes them in two levels.

- In the first level, estimate the intermediate velocity by overlooking the pressure.
- We obtained the updated velocity field in the second level using the pressure over the divergence-free space.

Now, we consider the NSE for the incompressible fluid flow as in Weinan and Liu (1995) is:

$$\begin{cases} \frac{\partial \mathbf{u}}{\partial t} + (\mathbf{u} \cdot \nabla)\,\mathbf{u} = -\frac{1}{\rho}\nabla p + \nu\,\nabla^2\mathbf{u} \\ \nabla \cdot \mathbf{u} = 0 \end{cases} \tag{24}$$

where, p is the pressure of the fluid, ρ is the fluid's density, ν is the kinematic viscosity of the fluid and $\mathbf{u} = (u_1, u_2)$. Here, in Eq. 24, we only use the Dirichlet boundary condition $\mathbf{u} = 0$ on $\partial\Omega = 0$, noticed that Ω is an unclosed domain in $\Re^2$.

In Level 1: Estimate the intermediate velocity $\mathbf{u}^*$ the first level by overlooking the pressure effect in Eq. 24. Mathematically, we have,

$$\frac{\partial \mathbf{u}}{\partial t} = -\,(\mathbf{u} \cdot \nabla)\,\mathbf{u} + \nu\,\nabla^2\mathbf{u} \tag{25}$$
$$\frac{\mathbf{u}^* - \mathbf{u}^n}{\Delta t} = -\,(\mathbf{u} \cdot \nabla)\,\mathbf{u} + \nu\,\nabla^2\mathbf{u} \tag{26}$$

Reorganizing Eq. 26 as:

$$\mathbf{u}^* = \mathbf{u}^n + \Delta t(-\,(\mathbf{u} \cdot \nabla)\,\mathbf{u} + \nu\,\nabla^2\mathbf{u}) \tag{27}$$

where, $\mathbf{u}^n$ is the velocity at n^{th} time-interval.

In Level 2: We now computed the final velocity of the fluid in the second level by iteratively improving the intermediate velocity $\mathbf{u}^*$ at $n + 1$-time intervals employing the mathematical relation as:

$$\mathbf{u}^{n+1} = \mathbf{u}^* - \frac{\Delta t}{\rho}\nabla p^{n+1} \tag{28}$$

where, $\mathbf{u}^{n+1}$ and ∇p^{n+1} are the updated final velocity and gradients of pressure at $n + 1$-time intervals.

The Eq. 28 can be rewritten as:

$$\begin{cases} \mathbf{u}^* = \mathbf{u}^{n+1} + \frac{\Delta t}{\rho}\nabla p^{n+1} \\ \nabla \cdot \mathbf{u}^{n+1} = 0 \end{cases} \tag{29}$$

Using the divergence-free condition $\nabla \cdot \mathbf{u}^{n+1} = 0$, we attain the pressure by taking the divergence on the right-hand side of Eq. 28 to derive the Poisson equation for the pressure at $n + 1$-time intervals denotes as p^{n+1}. Mathematically, written as:

$$\nabla^2 p^{n+1} = \frac{\rho}{\Delta t}\,\nabla \cdot \mathbf{u}^* \tag{30}$$

Rearranging Eq. 30 as:

$$\nabla^2 p^{n+1} - \frac{\rho}{\Delta t}\,\nabla \cdot \mathbf{u}^* = 0 \tag{31}$$

The fluid's density ρ and time-step Δt are constant, so we assume $\rho/\Delta t = a_0$, the Eq. 30 can be rewritten as follows:

$$\nabla^2 p^{n+1} = a_0\,\nabla \cdot \mathbf{u}^* \quad \therefore \; a_0 = \frac{\rho}{\Delta t} \tag{32}$$

Eq. 32 indicates the Poisson equation for the pressure at $n + 1$-time intervals. We apply the finite difference method to solve the Poisson equation to obtain pressure.

Consider R.H.S of Eq. 32, we have,

$$\nabla^2 p^{n+1} = p_{xx}^{n+1} + p_{yy}^{n+1} \tag{33}$$

$$\begin{cases} p_x^{n+1} = \frac{P_{i+1,j}^{n+1} - P_{i,j}^{n+1}}{h} \\ p_y^{n+1} = \frac{P_{i,j+1}^{n+1} - P_{i,j}^{n+1}}{k} \end{cases} \quad \text{(34-a), (34-b)}$$

$$\begin{cases} p_{xx}^{n+1} = \frac{P_{i-1,j}^{n+1} - 2\,P_{i,j}^{n+1} + P_{i+1,j}^{n+1}}{h^2} \\ p_{yy}^{n+1} = \frac{P_{i,j-1}^{n+1} - 2\,P_{i,j}^{n+1} + P_{i,j+1}^{n+1}}{k^2} \end{cases} \quad \text{(35-a), (35-b)}$$

Substitute Eq. 35-a and Eq. 35-b into Eq. 32 we have:

$$\nabla^2 p^{n+1} = a_0\,\nabla \cdot \mathbf{u}^*$$
$$p_{xx}^{n+1} + p_{yy}^{n+1} = a_0\,\nabla \cdot \mathbf{u}^*$$
$$\frac{P_{i-1,j}^{n+1} - 2\,P_{i,j}^{n+1} + P_{i+1,j}^{n+1}}{h^2} + \frac{P_{i,j-1}^{n+1} - 2\,P_{i,j}^{n+1} + P_{i,j+1}^{n+1}}{k^2} = a_0\,\nabla \cdot \mathbf{u}^* \tag{36}$$

We are working on the structured mesh therefore $h = k$ so, Eq. 36 becomes:

$$\frac{P_{i-1,j}^{n+1} + P_{i+1,j}^{n+1} + P_{i,j-1}^{n+1} + P_{i,j+1}^{n+1} - 4\,P_{i,j}^{n+1}}{h^2} = a_0\,\nabla \cdot \mathbf{u}^*$$
$$P_{i-1,j}^{n+1} + P_{i+1,j}^{n+1} + P_{i,j-1}^{n+1} + P_{i,j+1}^{n+1} - 4\,P_{i,j}^{n+1} = h^2\,a_0\,\nabla \cdot \mathbf{u}^* \tag{37}$$
$$P_{i-1,j}^{n+1} + P_{i+1,j}^{n+1} + P_{i,j-1}^{n+1} + P_{i,j+1}^{n+1} - 4\,P_{i,j}^{n+1} = h^2 F_{ih,jh} \quad \therefore \; F = a_0\,\nabla \cdot \mathbf{u}^* \tag{38}$$
$$P_{i-1,j}^{n+1} + P_{i+1,j}^{n+1} + P_{i,j-1}^{n+1} + P_{i,j+1}^{n+1} - h^2 F_{ih,jh} = 4\,P_{i,j}^{n+1} \tag{39}$$

Eq. 39 is the finite difference scheme for getting the pressure given in Eq. 32. If we set the boundary conditions over the boundary $\partial\Omega$ for pressure are $\nabla p^{n+1} \cdot \mathbf{n} = 0$, so Eq. 29 shows the typical Helmholtz-Hodge decomposition principle.

Practically, the boundary conditions $\nabla p^{n+1} \cdot \mathbf{n} = 0$ applied in this method causes errors due to the pressure from the actual solution of the Navier-Stoles equation that does not satisfy these conditions.

4. Test results and discussions

This section discusses the test results of the devised re-initialization scheme and examines the reversed vortex test instance.

4.1. Circular shape interface

In this test case, consider the computational domain $\Omega = [0\,,1] \times\ [0\,,1]$ with the center of a circle at point $(0.5,\ 0.5)^T$ and a radius of 0.25. The initial conditions of the LS field formulated in Eq. 40 for the circular shape interface are mathematically written as:

$$\phi(\boldsymbol{x}, 0) = |\boldsymbol{x} - \boldsymbol{x}^c(0)| - R \tag{40}$$

where, $\boldsymbol{x}^c(0) = (0.5, 0.5)^T$ denotes the center of the circle in Eq. 40.

Therefore, Fig. 3a and Fig. 3b depict the exact LS field (before re-initialization) and the re-initialized LS field (after re-initialization), respectively, over a circular shape interface.

4.2. Reversed vortex test case

The reversed vortex test instance is also the complex trial used for two-phase flow modeling for immiscible fluids because the divergence-free nonlinear velocity field distorts the interface and stretches out sharply throughout the advection process, causing an issue with actual mass conservation.

In this test instance, the computational domain $\Omega = [0\,,1] \times\ [0\,,1]$ consists of a circular fluid with its center initially located at $(0.5,\ 0.7)^T$ with a radius of. 0.16. The nonlinear divergence-free velocity field, as defined in Raees (2016), is employed for the advection of the circular region as follows:

$$u(\underline{x}, t) = \\ (sin^2(\pi x)\, sin(2\pi y), -sin^2(\pi y)\, sin(2\pi x))^{\,T} cos(\pi t/T), \\ \underline{x} \in \Omega, T \in [0\,,2] \tag{41}$$

According to the definition of the velocity field, the interface's location must revert to the exact initial location at the prescribed time $t = T$, which is also the actual time for the interface. In this instance, the cost of the specified time is $T = 2$. The exact LS (before re-initialization) and the re-initialized LS field (after re-initialization) at time t = 0 and time t = T are shown in Fig. 4a and Fig. 4b, respectively. The initial and final position of the LS field is depicted in Fig. 5 with three different mesh sizes h=100×100, 200×200, 400×400, at various time instances at time $t = 0$, $t = \frac{1}{4}T$, $t = \frac{1}{2}T$, $t = \frac{3}{4}T$ and $t = T$. This thorough analysis provides a comprehensive understanding of the LS field behavior over time.

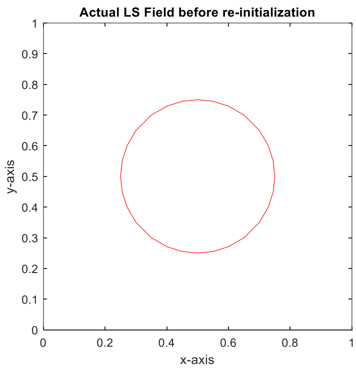

a: before re-initialization

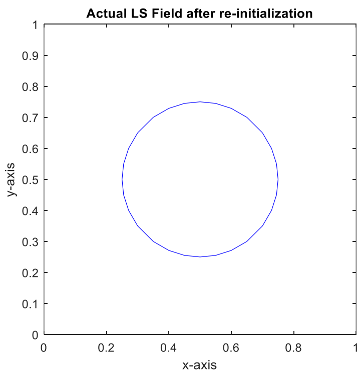

b: After re-initialization

Fig. 3: Contour plot of the exact LS field

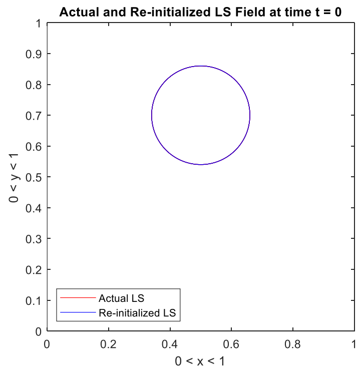

a: $t = 0$

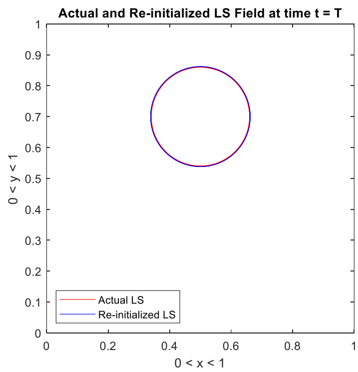

b: $t = T$

Fig. 4: The actual and re-initialized LS field

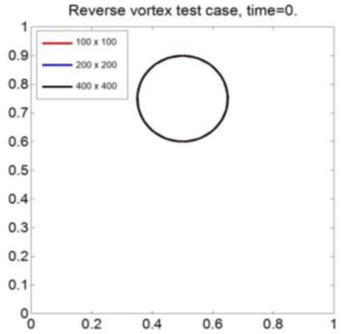

a: $t = 0$

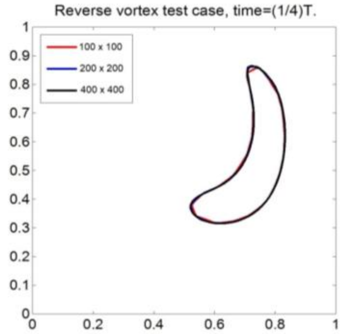

b: $t = \frac{1}{4}T$

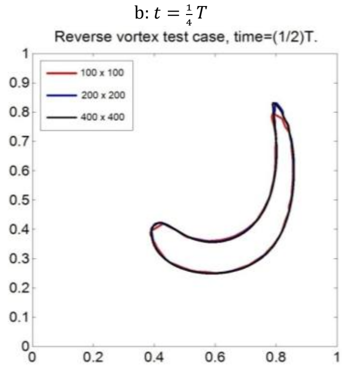

c: $t = \frac{1}{2}T$

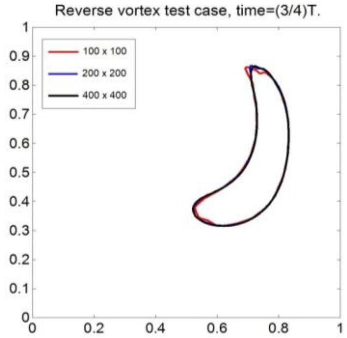

d: $t = \frac{3}{4}T$

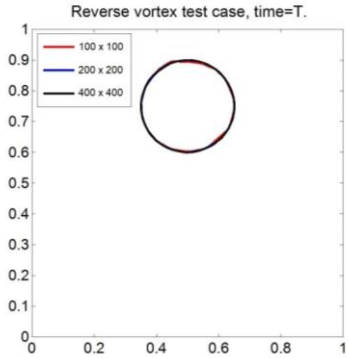

e: $t = T$

Fig. 5: The initial and final position of the LS field for the reverse vortex test case with different mesh sizes

4.3. Numerical simulation of lens-shaped interface deformation

In the starting, lens-shaped interface deformation is the most identified and continually employed benchmark for assessing the incompressible two-phase flow model. This benchmark depends on the liquid effects of the material, the density of the two-phase ratio, and the lens shape deviations from the outset to the end of the procedure.

In the computational domain $\Omega = [0\,,1] \times [0\,,1]$ we attain the LS field solution, the initial condition determined as:

$$\phi_l(\boldsymbol{G},0) = \max\,\{\phi_1(\boldsymbol{G},0), -\,\phi_2(\boldsymbol{G},0)\} \tag{42}$$

where,

$$\phi_1(\boldsymbol{G},0) = |\boldsymbol{G} - \boldsymbol{G}_1^e(0)| - N \tag{43}$$
$$\phi_2(\boldsymbol{G},0) = |\boldsymbol{G} - \boldsymbol{G}_2^e(0)| - N \tag{44}$$

Here we assume the simulated values as $\boldsymbol{G}_1^e(0) = (0.45, 0.15)^T$, $\boldsymbol{G}_2^e(0) = (0.45, 0.4)^T$, and $N = 0.25$. Therefore, Fig. 6a and Fig. 6b show the lens-shaped interface deformation before and after re-initialization, respectively.

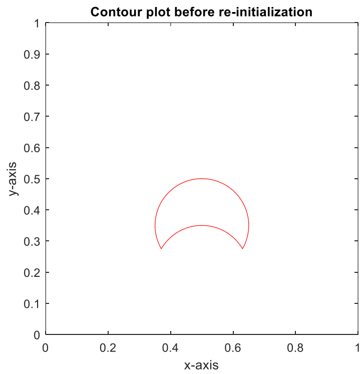

a: Before re-initialization

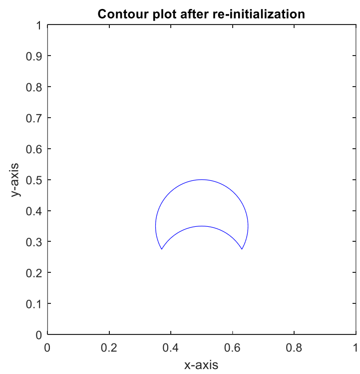

b: After re-initialization

Fig. 6: Lens-shaped interface deformation

4.4. Disc rotation case

In Zalesak's (1979) disc rotation, we examine the computational domain specified in the preceding test case. Now we state the initial condition for the LS field as,

$$\phi_l(\boldsymbol{G},0) = \max\,\{\phi_1(\boldsymbol{G},0), -\,\phi_2(\boldsymbol{G},0)\} \tag{45}$$

where,

$$\phi_1(\boldsymbol{G},0) = |\boldsymbol{G} - \boldsymbol{G}^e(0)| - N \quad (46)$$
$$\phi_2(\boldsymbol{G},0) = \max\ (|\mathbf{G}_1 - \mathbf{G}_1^e(0)| - n, |\mathbf{G}_2 - \mathbf{G}_2^e(0) + 2n| - d) \quad (47)$$

Here we assume the simulated values as $\boldsymbol{G}^e(0) = (0.45, 0.65)^T$, $N = 0.20$ and $\phi_2(\boldsymbol{G},0)$ comprise the rectangular region with breath $n = N/6$ and length $d = N$, respectively. Therefore, we diagrammatically display Zalesak's (1979) disc rotation before and after re-initialization in Fig. 7a and Fig. 7b, respectively.

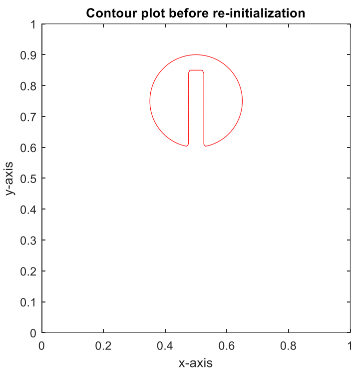

a: Before re-initialization

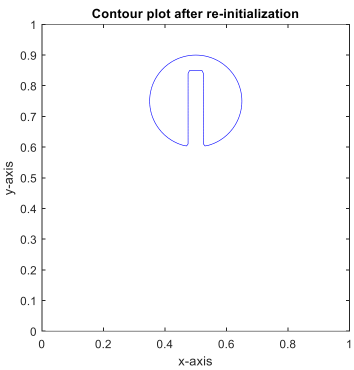

b: After re-initialization

Fig. 7: Zalesak's disc rotation

4.5. Error of the re-initialized LS field

This section presents the convergence and error associated with the re-initialized LS field in Table 1.

Table 1: Error and Convergence order of the re-initialized LS field

Mesh size	Max. error	Convergence order
100×100	2.1519e-04	-----
200×200	9.9739e-05	2.1575
400×400	4.7671e-05	2.0922

The LS function effectively re-initializes using Chorin's projection method with the solution of the Poisson equation, which is projected on the SD function. This method maintains smoothness but may raise a numerical error that needs a cautious parameter. Fast-marching and Hamilton-Jacobi solvers are the other re-initialization schemes in substitution. Still, the fast-marching re-initialization scheme may be numerically costly for complicated domains, and the Hamilton-Jacobi method can experience numerical diffusion in the re-initialization process.

The practical implementation challenges for LS re-initialization with Chorin's projection method are (i) it assures stability and conserving mass, specifically for irregular domains and coarse time intervals, (ii) accurately regulates boundary conditions, especially for complex geometries, (iii) for high-performance simulations, it successfully solves the Poisson equation that appears from the projection stage. All these difficulties may restrict the practical usage of the method, specifically in vast and real-time simulations.

Chorin's projection method solves the Poisson equation at each time interval during the re-initialization process, which could be computationally demanding, particularly for extensive 3D simulations. It acquires more iteration for convergence for complex geometries, which enriches its cost numerically. Discretization error, initial condition sensitivity, and complexities applying correct boundary conditions can cause convergence problems and imprecise solutions for complex geometries. In future research, the researchers may concentrate on these restrictions utilizing exact higher-order approaches, vigorous boundary conditions, dynamic grid adaptation, and high-performance solvers. Moreover, examining the hybrid methods merges the diverse re-initialization scheme's intensity, which might be the cause of optimal and more exact solutions.

5. Conclusion

This paper presents an effective re-initialization scheme for the Level-Set (LS) field by using Chorin's projection method. The Finite Element Method (FEM) framework is employed to solve the NSE numerically using the Chorin's projection method. The proposed scheme exhibits enhanced proficiency and effectiveness, ensuring accurate mass conservation of the LS. The proposed scheme's significance, efficiency, and effectiveness are valid through benchmark test cases. This research paper presents a conclusive and innovative solution for efficiently solving time-dependent incompressible fluid flow issues. The method utilizes Chorin's projection method to separate pressure and velocity fields and includes an efficient re-initialization scheme for the LS field. The study proves its accuracy, efficiency, and ability to conserve mass, making it a valuable contribution to numerical analysis and computational fluid dynamics. In future research, the investigators may precede this research for unstructured meshes to achieve the optimum order of convergence and high accuracy using the presented re-initialization scheme.

List of symbols

p	Pressure of the fluid
ρ	Fluid density
ν	Kinematic viscosity

ϕ	LS value/LS function
$\Gamma(t)$	Interface in time t
Ω	Bounded region/computationally domain
$\frac{\partial \phi}{\partial t}$	Interface varies with time t
$\mathbf{V}$	Divergence-free velocity field
$\nabla \phi$	Singed distance function gradients
N_i	Quadrilateral element shape functions
x_l *and* y_l	Node coordinates
x_L *and* y_L	Points positioned at the interface
λ	Lagrange multiplier
T	Transpose
d	Minimal interface distance and rectangular region length
ϕ'	Updated LS value
$\boldsymbol{u}_{sol.}$	The solenoidal portion of the velocity field
$\boldsymbol{u}_{irrot.}$	The irrotational portion of the velocity field
$\boldsymbol{u}^{n+1}$	Updated final velocity field at n+1- time intervals
∇p^{n+1}	Updated pressure gradients at n+1- time intervals
$\partial \Omega$	Boundary
$\phi(\boldsymbol{x}, 0)$	Initial conditions for the LS field
$\boldsymbol{x}^c(0)$	Center of the circle
$\boldsymbol{G}_1^c(0)$	Lens center
R and N	Circle and the lens radius
n	Rectangular region breath

Acknowledgment

This research was funded by the NED University of Engineering and Technology, Karachi, Pakistan. The author and co-author both are very thankful to NED University and acknowledged for their support.

Compliance with ethical standards

Conflict of interest

The author(s) declared no potential conflicts of interest with respect to the research, authorship, and/or publication of this article.

References

Akbar N, Hussain SM, and Khan RU (2022). Numerical solution of casson fluid flow under viscous dissipation and radiation phenomenon. Journal of Applied Mathematics and Physics, 10(2): 475-490. https://doi.org/10.4236/jamp.2022.102036

Ausas RF, Dari EA, and Buscaglia GC (2008). A mass-preserving geometry-based reinitialization method for the level set function. Mecánica Computacional, 27: 13-32.

Badia S and Codina R (2007). Convergence analysis of the FEM approximation of the first order projection method for incompressible flows with and without the inf-sup condition. Numerische Mathematik, 107: 533-557. https://doi.org/10.1007/s00211-007-0099-5

Bir B, Goswami D, and Pani AK (2024). Optimal error estimates of the penalty finite element method for the unsteady Navier–Stokes equations with nonsmooth initial data. Journal of Scientific Computing, 98: 51. https://doi.org/10.1007/s10915-023-02445-6

Bressan A (2011). Isogeometric regular discretization for the Stokes problem. IMA Journal of Numerical Analysis, 31(4): 1334-1356. https://doi.org/10.1093/imanum/drq014

Chan TF and Vese LA (2001). Active contours without edges. IEEE Transactions on Image Processing, 10(2): 266-277. https://doi.org/10.1109/83.902291 **PMid:18249617**

Chorin AJ (1967). The numerical solution of the Navier-Stokes equations for an incompressible fluid. Bulletin of the American Mathematical Society, 73(6): 928-931. https://doi.org/10.1090/S0002-9904-1967-11853-6

Chorin AJ (1997). A numerical method for solving incompressible viscous flow problems. Journal of Computational Physics, 135(2): 118-125. https://doi.org/10.1006/jcph.1997.5716

Chorin AJ and Marsden JE (1990). A mathematical introduction to fluid mechanics. Volume 3, Springer, New York, USA. https://doi.org/10.1007/978-1-4684-0364-0

Codina R (2001). Pressure stability in fractional step finite element methods for incompressible flows. Journal of Computational Physics, 170(1): 112-140. https://doi.org/10.1006/jcph.2001.6725

Dana S, Jammoul M, and Wheeler MF (2021). Performance studies of the fixed stress split algorithm for immiscible two-phase flow coupled with linear poromechanics. Computational Geosciences, 26: 13-27. https://doi.org/10.1007/s10596-021-10110-w

de Boor C (1978). A practical guide to splines. Volume 27, Springer-Verlag, New York, USA. https://doi.org/10.1007/978-1-4612-6333-3

de Frutos J, García-Archilla B, and Novo J (2018). Error analysis of projection methods for non inf-sup stable mixed finite elements: The Navier–Stokes equations. Journal of Scientific Computing, 74: 426-455. https://doi.org/10.1007/s10915-017-0446-3

Derr NJ and Rycroft CH (2022). A projection method for porous media flow. Arxiv Preprint Arxiv:2206.14379. https://doi.org/10.48550/arXiv.2206.14379

Gagniere S, Hyde D, Marquez-Razon A, Jiang C, Ge Z, Han X, Guo Q, and Teran J (2020). A hybrid Lagrangian/Eulerian collocated velocity advection and projection method for fluid simulation. Computer Graphics Forum, 39(8): 1-14. https://doi.org/10.1111/cgf.14096

Gharibi Z and Dehghan M (2024). Analysis of weak Galerkin mixed finite element method based on the velocity–Pseudostress formulation for Navier–Stokes equation on polygonal meshes. Journal of Scientific Computing, 101: 12. https://doi.org/10.1007/s10915-024-02651-w

Gresho PM and Sani RL (1987). On pressure boundary conditions for the incompressible Navier-Stokes equations. International Journal for Numerical Methods in Fluids, 7(10): 1111-1145. https://doi.org/10.1002/fld.1650071008

Guermond J and Shen J (2004). On the error estimates for the rotational pressure-correction projection methods. Mathematics of Computation, 73(248): 1719-1737. https://doi.org/10.1090/S0025-5718-03-01621-1

Guermond JL and Quartapelle L (1998). On the approximation of the unsteady Navier–Stokes equations by finite element projection methods. Numerische Mathematik, 80: 207-238. https://doi.org/10.1007/s002110050366

Han WW, Jiang YL, and Miao Z (2023). Numerical analysis of projection methods for the time-dependent Navier-Stokes equations with modular grad-div stabilization. Computers and Mathematics with Applications, 141: 145-158. https://doi.org/10.1016/j.camwa.2023.04.015

Hartmann D, Meinke M, and Schröder W (2008). Differential equation based constrained reinitialization for level set methods. Journal of Computational Physics, 227(14): 6821-6845. https://doi.org/10.1016/j.jcp.2008.03.040

Hirt CW and Nichols BD (1981). Volume of fluid (VOF) method for the dynamics of free boundaries. Journal of Computational Physics, 39(1): 201-225. https://doi.org/10.1016/0021-9991(81)90145-5

Jobelin M, Lapuerta C, Latché JC, Angot P, and Piar B (2006). A finite element penalty–projection method for incompressible flows. Journal of Computational Physics, 217(2): 502-518. https://doi.org/10.1016/j.jcp.2006.01.019

Karam M and Saad T (2023). On the theory of fast projection methods for high-order Navier-Stokes solvers. Journal of Computational Physics, 495: 112557. https://doi.org/10.1016/j.jcp.2023.112557

Khan W, Ullah B, and Ullah Z (2020). The localized radial basis functions for parameterized level set based structural optimization. Engineering Analysis with Boundary Elements, 113: 296-305. https://doi.org/10.1016/j.enganabound.2020.01.008

Long X and Ding Q (2023). Convergence analysis of the fully discrete projection method for inductionless magnetohydrodynamics system based on charge conservation. Journal of Scientific Computing, 96: 2. https://doi.org/10.1007/s10915-023-02226-1

Lyras KG, Hanson B, Fairweather M, and Heggs PJ (2020). A coupled level set and volume of fluid method with a re-initialisation step suitable for unstructured meshes. Journal of Computational Physics, 407: 109224. https://doi.org/10.1016/j.jcp.2019.109224

Osher S and Sethian JA (1988). Fronts propagating with curvature-dependent speed: Algorithms based on Hamilton-Jacobi formulations. Journal of Computational Physics, 79(1): 12-49. https://doi.org/10.1016/0021-9991(88)90002-2

Owkes M and Desjardins O (2013). A discontinuous Galerkin conservative level set scheme for interface capturing in multiphase flows. Journal of Computational Physics, 249: 275-302. https://doi.org/10.1016/j.jcp.2013.04.036

Raees F (2016). A mass-conserving hybrid interface capturing method for geometrically complicated domains. Ph.D. Dissertation, Delft University of Technology, Delft, Netherlands.

Rannacher R (1992). On Chorin's projection method for the incompressible Navier-Stokes equations. In: Heywood JG, Masuda K, Rautmann R, Solonnikov VA (Eds.), The Navier-Stokes equations II — Theory and numerical methods. Lecture Notes in Mathematics, Vol 1530. Springer, Berlin, Germany. https://doi.org/10.1007/BFb0090341

Rider WJ and Kothe DB (1995). A marker particle method for interface tracking. In the 6th International Symposium on Computational Fluid Dynamics, Lake Tahoe, USA: 976-981.

Weinan E and Liu JG (1995). Projection method I: Convergence and numerical boundary layers. SIAM Journal on Numerical Analysis, 32(4): 1017-1057. https://doi.org/10.1137/0732047

Yang J, Li Y, and Kim J (2024). A structure-preserving projection method with formal second-order accuracy for the incompressible Navier–Stokes equations. Communications in Nonlinear Science and Numerical Simulation, 133: 107963. https://doi.org/10.1016/j.cnsns.2024.107963

Zalesak ST (1979). Fully multidimensional flux-corrected transport algorithms for fluids. Journal of Computational Physics, 31(3): 335-362. https://doi.org/10.1016/0021-9991(79)90051-2

Zhang Y (2014). Fast approach to checkerboard corner detection for calibration. Optical Engineering, 53(11): 112203. https://doi.org/10.1117/1.OE.53.11.112203